Fatigue crack growth behavior of wire arc additively manufactured 316L austenitic stainless steel

Yangyu Chen [a, b], Man-Tai Chen [a, b, *], Ou Zhao [c], Barbara Rossi [d, e], Xiongfeng Ruan [d, e]

[a] *State Key Laboratory of Ocean Engineering, Shanghai Jiao Tong University, Shanghai 200240, China*
[b] *Shanghai Key Laboratory for Digital Maintenance of Buildings and Infrastructure, Department of Civil Engineering, Shanghai Jiao Tong University, Shanghai 200240, China*
[c] *School of Civil and Environmental Engineering, Nanyang Technological University, Singapore*
[d] *Department of Engineering Science, University of Oxford, Parks Road, Oxford OX1 3PJ, UK*
[e] *Faculty of Engineering Technology, KULeuven, Leuven, Belgium*

Abstract: This study investigated the fatigue crack growth (FCG) performance of 316L austenitic stainless steel produced by wire arc additive manufacturing (WAAM) through fatigue tests and fractographic analyses. A total of 11 compact tension (CT) specimens were designed considering three minimum-to-maximum load ratios (R = 0.1, 0.3, 0.5), various load directions (θ = 0°, 30°, 45°, 60°, 90°) and two surface conditions (milled and as-built). Details of specimen fabrication and design as well as fatigue test setup are presented. The Paris' law material constants of all specimens were derived. The influences of various parameters on the FCG behavior such as crack length development histories and fatigue crack growth rate (FCGR) are discussed. The test results demonstrated that the fatigue crack growth rate increased with the load ratio, and that the specimen with θ = 0°, i.e. load parallel to the welding pass, possessed higher FCGR value than the counterparts characterized by other load directions. The as-built and milled specimens had similar FCG performance. The FCG test results of WAAM 316L austenitic stainless steel obtained in this study were compared against those of 316L steels manufactured by traditional hot-rolling and selective laser melting as well as the predictions by current international standards (BS 7910 and IIW-1823-07). The fractographies of typical CT specimens from macroscopic and microscopic perspectives were analyzed. Transgranular fracture was observed as evidenced by abundant fatigue striations, secondary cracks and dimples.

Keywords: Austenitic stainless steel; Fatigue crack growth; Fractography; Metallic 3D printing; Wire arc additive manufacturing (WAAM).

* Corresponding author.

E-mail address: mantai.chen@sjtu.edu.cn (Man-Tai Chen)

1 Introduction

Metal additive manufacturing, commonly referred to as metal 3D printing, represents an innovative technological advancement whereby complex objects [1–4] and advanced materials [5–7] can be meticulously fabricated layer by layer utilizing metallic powder or filament as feedstock. Within the realm of metal 3D printing techniques, Wire Arc Additive Manufacturing (WAAM) emerges as a singular technique. Employing an electric arc as heat source, WAAM melts metal wires to deposit material layer by layer, enabling to form intricate three-dimensional structures [8]. Although the origin of WAAM dates back to 1926, it is only recently that this technique's compelling advantages start to be recognized by the industry, including remarkable wire feed utilization ratios, cost-effectiveness, streamlined production processes, and substantial potential for constructing large-scale steel structures with complex configurations promoting more rational use of materials, owing to its relatively high deposition rate and fewer limitations on building size. As a result, WAAM recently emerged as the premier 3D printing technology for applications within the construction industry. In the construction sector, WAAM exhibits immense potential across various applications such as joint manufacturing [9], component repair [10,11], and structural connection [12–15]. Through the utilization of WAAM, the construction industry is poised to experience transformative advancements, facilitating the creation of more robust, customized, and intricate structure.

To enable the more widespread integration of WAAM by the industry, it is imperative to conduct research on the mechanical behavior of WAAM structure. Recently studies have investigated the material properties of WAAM specimens under static loading [16–22]. Chen *et al.* [16–18] conducted uniaxial tensile tests and microscopic observations on WAAM high strength steel, austenitic stainless steel and duplex stainless steel specimens, discussing strength and material anisotropy. Huang *et al*. [21] analyzed the stress-strain responses of WAAM specimens made of normal-strength and high-strength steels collected from existing literature

based on which the developed new material constitutive models. Hadjipantelis *et al*. [22] proposed a new anisotropic material model for WAAM 308L stainless steel, where the orthotropic plane stress material model and Hill's yield criterion were adopted in the elastic and inelastic regions, respectively.

Designing steel structures against fatigue presents significant challenges. Under cyclic loading, fatigue failure mechanisms entail crack initiation, crack propagation, eventually followed by fracture [23]. Intrinsically different from e.g. hot-rolled metal, understanding and quantifying the fatigue crack growth (FCG) behavior of WAAM metals emerges as key to ensure the integrity and longevity of structures employing this technology. Huang *et al*. [24] investigated the effects of specimen thickness and load direction on the FCG properties of WAAM normal- and high-strength steels. Ermakova *et al*. [25,26] reported the FCG experimental results on WAAM carbon steels made using ER70S-6 and ER100S-1 wire feeds under different maximum loads. Gordon *et al*. [27] explored the impact of residual stresses on the FCG performance of WAAM 304L austenitic stainless steel. Nevertheless, today's research mainly concentrates on the FCG behavior of WAAM carbon steels, while those focusing on WAAM stainless steels are relatively scarce, and the effects of load ratio and surface undulation have, so far, not been investigated.

This study focuses on the FCG behavior of WAAM 316L austenitic stainless steel by means of fatigue tests and fractographic analyses. Different values of load ratio (R = 0.1, 0.3, 0.5), load direction (θ = 0°, 30°, 45°, 60°, 90°) and surface condition (milled and as-built) were considered and a total of 11 compact tension (CT) specimens were carried out. The paper provides details of the specimen fabrication, outlines the tensile material properties and presents the fatigue test setup. Based on the experimental results, the influence of load ratio, load direction and surface condition on the FCG behavior is discussed. The experimental results were then compared with those of 316L steels manufactured by traditional hot-rolling [28] and selective laser melting [29]

as well as the predictions by current international standards (BS 7910 [30] and IIW-1823-07 [31]). The macroscopic and microscopic fractographies of typical CT specimens were analyzed.

2 Specimen manufacturing

Commercial ER316L wire with 1.2 mm diameter was utilized to produce runway-shaped oval steel tubes atop a base plate (see Fig. 1) using wire arc additive manufacturing (WAAM). The chemical composition of the feedstock wire provided by the manufacturer is summarized in Table 1. The wire mill certificate tensile strength is 568 MPa and the elongation after fracture is 39%. The manufacturing process employed a KUKA six-axis robotic arm coupled with a Fronius TPS 400i metal inert gas torch. The filamentous materials were deposited in layer-by-layer, adopting the strategy of reversing the deposition direction for every layer. Key parameters used in the additive process are: wire feeding rate = 5 m/min, travel speed = 0.6 m/min, welding voltage = 19.6 V, welding current = 144 A, shielding gas made of 98% Ar + 2% CO_2 with a flow rate of 20 L/min. The flat portions of the runway-shaped oval steel tubes were 380 mm long by 380 mm high with a nominal thickness of 6.5 mm. The printed oval tubes were cut off from the base plate at a distance of 5 mm through wire cutting. Subsequently, the extracted flat steel plates were used to manufacture the test specimens.

To study the FCG behavior of the WAAM 316L austenitic stainless steel, CT specimens were designed following the guideline of ASTM E647 [32] with detailed dimensions as shown in Fig. 2 (a). Two circular holes with a diameter of 12.5 mm were designed to cater for the load application in the testing device. The horizontal distance between the center of the circular hole and the specimen's edge (W) as depicted in Fig. 2 (a) was set to 50 mm. To facilitate fatigue crack initiation, a spike-shaped notch was designed, with the distance from the center of circular hole to the notch tip (a_n) being 10 mm. A 5 mm wide knife edge was incorporated at the notch mouth to facilitate the installation of clip gauge to monitor the crack length based on the compliance

method. The CT specimens with notch, knife edge and two circular holes were manufactured from WAAM steel plates by electrical discharge machining (EDM).

It was stated in previous research studies [33–35] that the fatigue crack growth rate (FCGR) of steel is influenced by the minimum-to-maximum load ratio $R = P_{min}/P_{max}$ under cyclic loading. In this study, three different values of the load ratio (R = 0.1, 0.3, 0.5) were adopted, which fall within the typical range of the load ratio in practical engineering structures subjected to cyclic loading [23] and have been widely employed in the FCG tests of various steel materials [33–35]. Since the mechanical properties of WAAM stainless steels exhibit variations across different load directions relative to the deposition direction [22], five load directions (θ = 0°, 30°, 45°, 60°, 90°), which have been utilized to explore the potential influence of material anisotropy [16–18,21], were selected in this study as shown in Fig. 2 (b). In addition, both milled CT specimen with smooth surface and as-built specimen with inherent undulating surface were considered to analyze the effect on FCG behavior. A total of 11 CT specimens were designed and manufactured. The thickness of the milled CT specimens was measured using a vernier caliper, while the detailed geometries of as-built specimen were measured by 3D laser scanning method using a FARO Quantum Max ScanArm based on which the mean thickness was calculated. The measured thickness (B) of each WAAM 316L austenitic stainless steel CT specimen is reported in Table 2.

The labelling of each CT specimens is described as follows. The first number in the designation represents the wire material ER316L used in this study. The second character indicates the surface condition of the specimen (M = Milled specimen, AB = As-Built specimen). After the first two symbols, the load direction θ in degree (θ = 0°, 30°, 45°, 60°, 90°) and the load ratio R (R = 0.1, 0.3, 0.5) are provided, respectively. The symbol “#” denotes a repeated test.

3 Tensile coupon tests

The static material properties of milled and as-built WAAM 316L austenitic stainless steel specimens were determined by tensile coupon tests considering five load directions (θ = 0°, 30°, 45°, 60°, 90°). The coupons were designed as per the ASTM E8/E8M [36] and loaded by a universal tensile testing machine. The static stress-strain responses were obtained, from which the mechanical parameters including Young's modulus E, yield stress f_y (taken as the 0.2% proof stress), ultimate strength f_u, ultimate strain ε_u and fracture strain ε_f were derived. Surface roughness typically has little effect on the intrinsic material property. However, the average cross-sectional area was used to derive the stress and strain, as reported in Zuo *et al*. [12]. Therefore, for tensile coupon with loading direction perpendicular to the printing direction, the roughness entails larger deformation and material properties lower than those measured for milled counterparts. Additionally, the results showed a certain degree of material anisotropy as evidenced by higher values of E, f_y and f_u for coupons with θ = 30°, 45°, 60° but lower ultimate and fracture strains, than for those with θ = 0° and 90°. The coupon test results have been reported in detail by Zuo *et al*. [12], and a summary of static material properties of WAAM 316L austenitic stainless steel related to this study is listed in Table 3.

4 Fatigue crack growth tests

4.1 Test details

The fatigue crack growth (FCG) tests were performed using an MTS 370 electro-hydraulic servo fatigue testing machine based on the ASTM E647 [32]. In engineering structures, natural fatigue cracks develop gradually under service loads, creating sharp crack tips with distinct microstructural features — unlike machined notches which are relatively blunt and affected by fabrication processes. Therefore, before the formal FCG test, pre-cracking was conducted to alleviate the impact of the notch fabrication process and to generate an initial crack that better

represents realistic conditions. The length of the pre-crack was set to 3 mm, which is the maximum value among 0.1 times the thickness of CT specimen, the width of the notch (3 mm) and 1 mm, in accordance with the ASTM E647 [32]. The maximum load P_{max} was firstly determined during the pre-cracking stage such that the fatigue crack growth rate (FCGR) was stabilized between 1.0×10^{-5} and 2.5×10^{-5} mm/cycle. In this study, a load-controlled sinusoidal cyclic loading scheme with a maximum load P_{max} of 5.4 kN and a frequency of 10 Hz was employed for all WAAM 316L austenitic stainless steel CT specimens during pre-cracking and formal FCG test stages. It should be mentioned that the number of load cycles required to generate the pre-crack is not included in the FCG result discussion.

To monitor the development of fatigue crack length, two methods, namely compliance method and optical method were employed. The fatigue crack growth histories of two WAAM 316L steel CT specimens (316-M-0-0.1 and 316-M-90-0.1#) were captured by optical method with the assistance of a travelling microscope (JCXE-DK). Whereas the fatigue crack growth of the remaining nine CT specimens was monitored by compliance method using an MTS model 632.03F-30 clip gauge installed at the notch mouth. The crack mouth opening displacement (CMOD) was directly measured by the clip gauge and further converted into a crack length. The experimental setups for the two measuring methods are shown in Fig. 3. The WAAM 316L steel CT specimens were loaded until the specimens reached the stage of rapid crack propagation [24] characterized by an ultimate crack length around 30 mm. The crack length a and the corresponding number of load cycles N were recorded at around 0.25 mm crack length growth interval according to the ASTM E647 [32]. After the FCG tests, the uncracked ligament of each CT specimen was pulled apart by monotonic tensile loading for subsequent morphological characteristics observation of the fracture surface.

4.2 Results and discussions

The initial fatigue crack length was set to 13 mm as determined by the sum of the notch length and pre-crack length. From then on, the crack length versus the corresponding number of load cycles responses (*a*-*N* curves) of all 11 WAAM 316L austenitic stainless steel CT specimens are plotted as displayed in Fig. 4. The fatigue crack growth path of a typical specimen 316-M-0-0.1 captured by optical method using a travelling microscope and the surface cracks images on the specimen at different crack lengths are depicted in the corresponding *a*-*N* curve as shown in Fig. 5. Besides the *a*-*N* curve, the fatigue crack growth rate d*a*/d*N* is another key result that reflects the FCG behavior. The fatigue crack growth rate (FCGR) of each WAAM 316L stainless steel CT specimen was determined based on the corresponding *a*-*N* data through secant method, as recommended by the ASTM E647 [32] and expressed in Eq (1).

$$\left(\frac{\mathrm{d}a}{\mathrm{d}N}\right)_i = \frac{a_{i+1} - a_i}{N_{i+1} - N_i} \tag{1}$$

where a is the crack length, N denotes the number of load cycles, and subscript i represents the i^{th} recorded data.

To describe the stress state at the crack tip, the stress intensity factor range ΔK for each loading cycle was calculated according to ASTM E647 [32] as provided in Eq. (2).

$$\Delta K = \frac{\Delta P}{B\sqrt{W}} \frac{(2+\alpha)}{(1-\alpha)^{1.5}} (0.886 + 4.64\alpha - 13.32\alpha^2 + 14.72\alpha^3 - 5.6\alpha^4) \tag{2}$$

where ΔP represents the load range in one cycle ($\Delta P = P_{max} - P_{min}$), B and W are the dimensions of the CT specimen defined in Fig. 2 (a), α equals to a / W, where a is the crack length.

Based on Paris' law [37], the relationship between the FCGR (d*a*/d*N*) and the stress intensity factor range (ΔK) in the crack stable growth stage can be expressed by Eq. (3). By taking the logarithm, Eq. (3) can be converted into Eq. (4).

$$\frac{\mathrm{d}a}{\mathrm{d}N} = C(\Delta K)^m \tag{3}$$

$$\log(\frac{\mathrm{d}a}{\mathrm{d}N}) = m\log(\Delta K) + \log C \quad (4)$$

where C and m are material constants which characterize the FCG performance.

The values of da/dN (in mm/cycle) and ΔK (in MPa·mm$^{1/2}$) were computed and used to derive the two material constants C and m through the least squares method as reported in Table 2. The da/dN-ΔK data and the corresponding fitted lines for all WAAM 316L stainless steel CT specimens are plotted in double logarithmic coordinate in Fig. 6. The actual ultimate crack length a_u of each WAAM 316L stainless steel CT specimen is presented in Table 2.

4.2.1 Effect of load ratio

The fatigue crack length versus number of cycles (a-N) responses of WAAM 316L austenitic stainless steel subjected to different load ratios (R = 0.1, 0.3, 0.5) are presented in Fig. 4 (a) and (b) for CT specimens with load direction θ = 0° and 90°, respectively. As expected, with increased load ratio, the required number of load cycles needed to achieve the same crack length increases. The corresponding FCGR and stress intensity factor range (da/dN-ΔK) responses for CT specimens subjected to different load ratios during crack stable growth stage are depicted in Fig. 6 (a) and (b). The fitted values of material constants C and m based on Paris' law [37] are shown in Table 2. To investigate the effect of load ratio on FCGR behavior and facilitate direct comparison, a regression analysis was conducted again to fit the data of da/dN and ΔK with a fixed value of the slope m. This value is predetermined by averaging all obtained m values for the specimens in the same group, but with different load ratios (m equals to 4.04 and 3.82 for specimen groups 316-M-0-R and 316-M-90-R, respectively). The re-fitted results are reported in Table 4. It is apparent that, under the same ΔK, the FCGR increases with the load ratio as evidenced by the higher value of material constant C.

Although Paris' law has been widely employed to describe the FCG performance of various materials, the effect of the load ratio is not considered in the formula. A load ratio factor was proposed by Walker [38] in a modified Paris' law equation expressed by Eq. (5). By taking the

logarithm on both sides, Eq. (5) can be converted into Eq. (6), where C, n, m are material constants.

$$\frac{da}{dN} = C(1-R)^n(\Delta K)^m \tag{5}$$

$$\log\left(\frac{da}{dN}\right) = \log C + n\log(1-R) + m\log(\Delta K) \tag{6}$$

A regression analysis was conducted accordingly against the results as shown in Fig. 7 and Table 5. It is shown that the effect of the load ratio on the FCGR for the CT specimens with load direction θ = 0° was more significant than that with θ = 90°, with an absolute value of constant n of the former group ($|n|$ =1.31) larger than that of the latter ($|n|$ = 0.70).

4.2.2 Effect of load direction

The FCG behavior (a-N and da/dN-ΔK responses) of WAAM 316L austenitic stainless steel CT specimens with different load directions and R = 0.1 are presented in Fig. 4 (c) and Fig. 6 (c). It can be observed from Fig. 4 (c) that to achieve the same crack length, the required number of load cycles is maximum for θ = 60° (indicating slow FCGR) and minimum for θ = 0° and 30°. To facilitate the direct analysis, the da/dN and ΔK datasets for all 316-M-θ-0.1 specimens during the crack stable growth stage were fitted with a fixed value of the slope m, predetermined by averaging the m values obtained for all specimens in the same group but different load directions. It can be observed from Table 6 that with θ = 60° the slowest FCGR was obtained whereas with θ = 0° the fastest FCGR was obtained, as evidenced by the values of the material constant C, respectively, indicating a certain degree of anisotropy on the FCG behavior for WAAM 316L austenitic stainless steel.

4.2.3 Effect of surface condition

The a-N and da/dN-ΔK responses of WAAM 316L austenitic stainless steel CT specimens

with milled and as-built surfaces (316-M-0-0.1 and 316-AB-0-0.1) are plotted in Fig. 4 (d) and Fig. 6 (d). It can be observed that to achieve the same crack length, the required number of load cycles for as-built CT specimen 316-AB-0-0.1 was larger than that for milled counterpart 316-M-0-0.1, which may be due to the larger thickness B of the as-built specimen resulting in a smaller value of the stress intensity factor range ΔK in each load cycle. It can be observed from Table 2 and Fig. 6 (d) that, under the same ΔK, the milled and as-built CT specimens have similar FCG performance in terms of FCGR. A reasonable explanation is that both the milled and as-built CT specimens possess the same notch shape, and even though they have different surface roughness, the local stress concentration at the crack tip governs the fatigue behavior.

4.2.4 Comparisons with hot-rolled and SLM 316L stainless steels as well as standards

The FCG test results of WAAM 316L austenitic stainless steel were compared with those of 316L steels manufactured by traditional hot-rolling [28] and selective laser melting [29] as well as the predictions by current international standards (BS 7910 [30] and IIW-1823-07 [31]). To facilitate direct comparison, the two material constants in Paris' law (C and m) of WAAM 316L stainless steel in this study were derived based on the datasets of the specimen group 316-M-θ-0.1 with the load ratio R = 0.1 and are compared against those in existing literature [28,29] and international standards (BS 7910 [30] and IIW-1823-07 [31]), see Table 7. The corresponding da/dN–ΔK curves are plotted in Fig. 8. The comparison on the FCG resistance of different steels can be analyzed through the relative position of the curves (i.e. the lower position of the curve indicates the better FCG resistance of the corresponding steel material), and the curve of the studied WAAM steel is at the lowest position. Therefore, it can be inferred that WAAM 316L austenitic stainless steel generally displayed greater FCG resistance than those manufactured by traditional hot-rolling, selective laser melting, or than the standardized predictions, i.e. lower FCGR. A possible explanation is that the WAAM process can result in much more irregular grain

shape of steel material, exhibiting interlocking basket weave structures. This can cause multiple deviations of the crack path along the main propagation direction, and thus reducing the FCGR [39].

5 Fracture surface analyses

To further understand the fatigue crack growth mechanism of WAAM 316L austenitic stainless steel, the fractographies of typical CT specimens (316-M-0-0.1 and 316-M-90-0.1#) from macroscopic and microscopic perspectives were analyzed. The macroscopic fractographies shown in Fig. 9 display a fracture surface clearly divided into two zones: the fatigue crack growth region and the fast fracture zone formed by monotonic tensile loading. The surface in the fast fracture zone is coarser than in the fatigue crack growth region, indicating that the former has undergone plastic deformation. Fractographies of typical CT specimens from microscopic perspective were observed by COXEM EM-30AX Plus scanning electron microscope. Micrographs of typical specimens taken at three crack lengths (a = 14, 21 and 28 mm) with two different magnifications (×200 and ×1000) are shown in Fig. 10 and Fig. 11. Fatigue striations, secondary cracks and dimples on the fracture surfaces were observed, inferring transgranular fracture. Fatigue striations can be distinguished as a series of parallel lines, whose distribution reveals the FCG direction and FCGR. The fatigue striations are approximately perpendicular to the crack growth direction, and their spacing increases with the FCGR. It can be observed from Fig. 10 and Fig. 11 that the fatigue striation spacing of specimen 316-M-0-0.1 is wider and more noticeable than that of specimen 316-M-90-0.1#, indicating that the former has a higher FCGR. Such observation conforms to the results shown in Table 6. Secondary crack associated with energy dissipation mainly orients perpendicular to the FCG direction. It can be found that specimen 316-M-90-0.1# possessed wider and longer secondary cracks than specimen 316-M-0-0.1, indicating more energy dissipation and thereby relatively slower FCGR for specimen 316-M-

90-0.1#, consistent with the FCG test results. Dimpled features were observed in high ΔK region (crack length a = 28 mm) for both specimens, demonstrating ductile fracture.

6 Conclusions

This study investigated the FCG performance of wire arc additively manufactured 316L austenitic stainless steel through fatigue tests and fractographic analyses. A total of 11 compact tension (CT) specimens were tested considering three load ratios (R = 0.1, 0.3, 0.5), five load directions (θ = 0°, 30°, 45°, 60°, 90°) and two surface conditions (milled and as-built). Fractographic analyses were conducted on two typical specimens.

(i) As expected, the fatigue crack growth rate (FCGR) increased with the load ratio. Additionally, the effect of the load ratio on the FCGR for CT specimen group with load direction θ = 0° (parallel to the deposition direction) was more significant than that with θ = 90°.

(ii) A certain degree of anisotropy was observed for the FCG behavior of WAAM 316L austenitic stainless steels. Specimen with θ = 60° in this study had the minimal FCGR and specimen with θ = 0° had the maximum FCGR.

(iii) Interestingly, the as-built and milled specimens had similar FCGR.

(iv) The WAAM 316L austenitic stainless steel in this study generally had greater FCG resistance than those manufactured by traditional hot-rolling or selective laser melting. Likewise, a comparison against standardized predictions from BS 7910 [18] and IIW-1823-07 [19], indicate that WAAM specimens have lower FCGR.

(v) The macroscopic and microscopic fractographies were analyzed for typical WAAM 316L austenitic stainless steel specimens. Two zones namely the fatigue crack growth region and the fast fracture zone were observed. Abundant fatigue striations, secondary cracks and dimples were found, indicating transgranular fracture of typical CT specimens.

Acknowledgements

The authors are grateful to Rongsu Technology Ltd. in China for supplying the test specimens. The authors gratefully acknowledge the financial support provided by the National Natural Science Foundation of China (No. 52378167 and No. 52108157), and the Shanghai Rising-Star Program, China (No. 24QA2704400).

Data Availability Statement

All data, models, and code generated or used during the study are available upon reasonable request.

Reference

[1] Zuo W, Chen MT, Chen Y, Zhao O, Cheng B, Zhao J. Additive manufacturing oriented parametric topology optimization design and numerical analysis of steel joints in gridshell structures. Thin-Walled Structures 2023;188:110817.

[2] Chen MT, Zuo W, Chen Y, Zhao O, Cheng B, Zhao J. Parametric topology optimization design and analysis of additively manufactured joints in spatial grid structures. Engineering Structures 2024;300:117123.

[3] Guo Q, Ye J, Lu H, Quan G, Wang Z, Zhao Y, Xie Y. Design and validation of 3D self-supporting structures and printing paths for multi-axis additive manufacturing. Additive Manufacturing 2024;96:104563.

[4] Yang L, Li Y, Chen Y, Yan C, Liu B, Shi Y. Topologically optimized lattice structures with superior fatigue performance. International Journal of Fatigue 2022;165:107188.

[5] Yang L, Wu S, Yan C, Chen P, Zhang L, Han C, Cai C, Wen S, Zhou Y, Shi Y. Fatigue properties of Ti-6Al-4V Gyroid graded lattice structures fabricated by laser powder bed fusion with lateral loading. Additive Manufacturing 2021;46:102214.

[6] Yang L, Yan C, Cao W, Liu Z, Song B, Wen S, Zhang C, Shi Y, Yang S. Compression-

compression fatigue behaviour of gyroid-type triply periodic minimal surface porous structures fabricated by selective laser melting. Acta Materialia 2019;181:49–66.

[7] Yang L, Mertens R, Ferrucci M, Yan C, Shi Y, Yang S. Continuous graded Gyroid cellular structures fabricated by selective laser melting: Design, manufacturing and mechanical properties. Materials & Design 2019;162:394–404.

[8] Gardner L. Testing and initial verification of the world's first metal 3D printed bridge. Journal of Constructional Steel Research 2020;172:106233.

[9] Laghi V, Babovic N, Benvenuti E, Kloft H. Blended structural optimization of steel joints for Wire-and-Arc Additive Manufacturing. Engineering Structures 2024;300:117141.

[10] Ghafoori E, Dahaghin H, Diao C, Pichler N, Li L, Mohri M, Ding J, Ganguly S, Williams S. Fatigue strengthening of damaged steel members using wire arc additive manufacturing. Engineering Structures 2023;284:115911.

[11] Du X, Shen Y, Zhao W, Chen J, Liu R, Wei Y. Wire arc additive manufacturing from the perspective of remanufacturing: A review of data processing. Journal of Manufacturing Processes 2023;107:385–410.

[12] Zuo W, Chen MT, Zhao O, Su A, Liu SW, Xu F, Huang Y, Cheng B. Behavior of wire arc additively manufactured 316L austenitic stainless steel single shear bolted connections. Thin-Walled Structures 2024;202:112075.

[13] Zuo W, Chen MT, Zhao O, Su A, Liu SW, Yun X, Xu F. Structural performance of wire arc additively manufactured duplex stainless steel single-lap shear bolted connections. Engineering Structures 2024;319:118706.

[14] Zuo W, Chen MT, Liu SW, Yun X, Zhao O, Huang Y, Cheng B. Experimental investigation on double-lap shear behavior of 3D printed austenitic stainless steel bolted connections. Engineering Structures 2024;317:118501.

[15] Zuo W, Chen MT, Zhao O, Gardner L. Testing of wire arc additively manufactured duplex stainless steel double-lap shear bolted connections. Journal of Structural Engineering 2025;151(2):04024205.

[16] Chen MT, Zhang T, Gong Z, Zuo W, Wang Z, Zong L, Zhao O, Hu L. Mechanical properties and microstructure characteristics of wire arc additively manufactured high-strength steels. Engineering Structures 2024;300:117092.

[17] Chen MT, Gong Z, Zhang T, Zuo W, Zhao Y, Zhao O, Zhang G, Wang Z. Mechanical behavior of austenitic stainless steels produced by wire arc additive manufacturing. Thin-Walled Structures 2024;196:111455.
[18] Chen MT, Chen Y, Zuo W, Yun X, Zhao O, Liu SW, Xu F. Experimental investigation on the tensile behavior of wire arc additively manufactured duplex stainless steel plates. Engineering Structures 2024;321:118764.
[19] Kyvelou P, Slack H, Daskalaki Mountanou D, Wadee MA, Britton TB, Buchanan C, Gardner L. Mechanical and microstructural testing of wire and arc additively manufactured sheet material. Materials & Design 2020;192:108675.
[20] Huang C, Kyvelou P, Zhang R, Ben Britton T, Gardner L. Mechanical testing and microstructural analysis of wire arc additively manufactured steels. Materials & Design 2022;216:110544.
[21] Huang C, Kyvelou P, Gardner L. Stress-strain curves for wire arc additively manufactured steels. Engineering Structures 2023;279:115628.
[22] Hadjipantelis N, Weber B, Buchanan C, Gardner L. Description of anisotropic material response of wire and arc additively manufactured thin-walled stainless steel elements. Thin-Walled Structures 2022;171:108634.
[23] Huang C, Li L, Pichler N, Ghafoori E, Susmel L, Gardner L. Fatigue testing and analysis of steel plates manufactured by wire-arc directed energy deposition. Additive Manufacturing 2023;73:103696.
[24] Huang C, Zheng Y, Chen T, Ghafoori E, Gardner L. Fatigue crack growth behaviour of wire arc additively manufactured steels. International Journal of Fatigue 2023;173:107705.
[25] Ermakova A, Mehmanparast A, Ganguly S, Razavi N, Berto F. Fatigue crack growth behaviour of wire and arc additively manufactured ER70S-6 low carbon steel components. International Journal of Fracture 2022;235(1):47–59.
[26] Ermakova A, Ganguly S, Razavi N, Berto F, Mehmanparast A. Experimental investigation of the fatigue crack growth behavior in wire arc additively manufactured ER100S-1 steel specimens. Fatigue & Fracture of Engineering Materials & Structures 2022;45(2):371–385.
[27] Gordon JV, Haden CV, Nied HF, Vinci RP, Harlow DG. Fatigue crack growth anisotropy, texture and residual stress in austenitic steel made by wire and arc additive manufacturing.

Materials Science and Engineering: A 2018;724:431–438.
[28] Feng G, Gong DW, Zhang CG, Han CJ, Lin KW, Qi JB. Experiment of fatigue crack growth behavior of 316L stainless steel (in Chinese). Iron and Steel 2014;49(6):74-78.
[29] Suryawanshi J, Prashanth KG, Ramamurty U. Mechanical behavior of selective laser melted 316L stainless steel. Materials Science and Engineering: A 2017;696:113–121.
[30] BS 7910:2019 Guide to methods for assessing the acceptability of flaws in metallic structures. BSI (British Standards Institution), Brussels, 2019.
[31] Hobbacher AF. Recommendations for Fatigue Design of Welded Joints and Components. International Institute of Welding, XIII-1823-07, Cham, Switzerland, 2008.
[32] ASTM E647-15 Standard test method for measurement of fatigue crack growth rates. ASTM International, West Conshohocken, PA, 2015.
[33] Zong L, Shi G, Wang Y. Experimental investigation and numerical simulation on fatigue crack behavior of bridge steel WNQ570 base metal and butt weld. Construction and Building Materials 2015;77:419–429.
[34] Su H, Wang J, Du J. Experimental and numerical study of fatigue behavior of bridge weathering steel Q345qDNH. Journal of Constructional Steel Research 2019;161:86–97.
[35] Xu Y, Li Z, Xu J, Han Q. Fatigue crack growth of G20Mn5QT cast steel based on a two-parameter driving force model. Engineering Fracture Mechanics 2019;208:13–26.
[36] ASTM E8/E8M - 22. Standard Test Methods for Tension Testing of Metallic Materials. ASTM International, West Conshohocken, PA, 2022.
[37] Paris P, Erdogan F. A Critical Analysis of Crack Propagation Laws. Journal of Basic Engineering 1963;85(4):528–533.
[38] Walker K. The Effect of Stress Ratio During Crack Propagation and Fatigue for 2024-T3 and 7075-T6 Aluminum. Effects of Environment and Complex Load History on Fatigue Life, ASTM International100 Barr Harbor Drive, PO Box C700, West Conshohocken, PA 19428-2959, 1970.
[39] He J, Feng X, Wang X, Guan X. Fatigue performance and acoustic emission behavior of remanufactured low-carbon steel made by wire and arc additive manufacturing. International Journal of Fatigue 2022;165:107190.

Table 1 The chemical composition of ER316L feedstock wire (in % by weight)

Feedstock wire	C	S	Mn	Si	P	Cr	Ni	Mo	Cu
ER316L	0.011	0.011	2.00	0.60	0.02	19.0	11.7	2.15	0.05

Table 2 Fatigue crack growth results of WAAM 316L stainless steel CT specimens

Specimen	B (mm)	Load range (kN)	a_u (mm)	C	m	R^2
316-M-0-0.1	5.05	4.86	28.31	1.62×10^{-16}	4.01	0.94
316-M-0-0.3	4.98	3.78	29.95	1.01×10^{-16}	4.11	0.98
316-M-0-0.5	4.99	2.70	31.48	3.09×10^{-16}	4.02	0.99
316-M-30-0.1	5.08	4.86	28.86	2.39×10^{-16}	3.94	0.99
316-M-45-0.1	5.04	4.86	29.44	9.36×10^{-16}	3.71	0.97
316-M-60-0.1	5.08	4.86	29.73	1.07×10^{-15}	3.67	0.95
316-M-90-0.1	4.98	4.86	28.11	1.29×10^{-15}	3.66	0.92
316-M-90-0.1#	4.94	4.86	31.40	8.17×10^{-18}	4.37	0.93
316-M-90-0.3	4.91	3.78	31.48	2.56×10^{-16}	3.91	0.92
316-M-90-0.5	5.09	2.70	31.35	1.84×10^{-14}	3.31	0.92
316-AB-0-0.1	6.75	4.86	31.46	2.39×10^{-16}	3.96	0.97

Table 3 Summary of tensile mechanical properties of WAAM 316L austenitic stainless steel [12]

θ (°)	Surface condition	E (GPa)	f_y (MPa)	f_u (MPa)	ε_u (%)	ε_f (%)
0	Milled	131.0	300.3	513.2	37.0	46.6
30	Milled	163.1	355.8	550.0	24.3	26.4
45	Milled	164.9	351.9	547.1	27.8	28.2
60	Milled	194.0	348.7	535.2	29.0	30.0
90	Milled	133.2	316.2	515.5	38.2	50.4
0	As-built	152.2	295.7	502.4	36.0	47.1

Table 4 Paris' law material constants of specimens with various load ratios derived based on a fixed value of *m*

Specimen	*C*	*m*	R^2
316-M-0-0.1	1.44×10^{-16}	4.04	0.93
316-M-0-0.3	1.91×10^{-16}	4.04	0.97
316-M-0-0.5	2.69×10^{-16}	4.04	0.99
316-M-90-0.1	4.34×10^{-16}	3.82	0.92
316-M-90-0.1#	5.33×10^{-16}	3.82	0.90
316-M-90-0.3	5.60×10^{-16}	3.82	0.91
316-M-90-0.5	6.21×10^{-16}	3.82	0.92

Table 5 Material constants in the model considering load ratio effect

Specimen group	Log *C*	*n*	*m*	R^2
316-M-0-*R*	-15.98	-1.31	4.05	0.98
316-M-90-*R*	-15.06	-0.70	3.70	0.94

Table 6 Paris' law material constants of specimens with various load directions derived based on a fixed value of *m*

Specimen	*C*	*m*	R^2
316-M-0-0.1	4.15×10^{-16}	3.89	0.93
316-M-30-0.1	3.46×10^{-16}	3.89	0.99
316-M-45-0.1	2.50×10^{-16}	3.89	0.97
316-M-60-0.1	2.35×10^{-16}	3.89	0.95
316-M-90-0.1	2.56×10^{-16}	3.89	0.92
316-M-90-0.1#	3.13×10^{-16}	3.89	0.90

Table 7 Paris' law material constants of 316L stainless steels by different manufacturing processes and current international standards

Source	Manufacturing process	*C*	*m*
This study	WAAM	5.24×10^{-16}	3.80
Suryawanshi [29]	Selective laser melting (SLM)	1.91×10^{-16}	4.02
Feng [28]	Hot-rolling	4.43×10^{-14}	3.45
BS 7910 [30]	-	3.98×10^{-13}	2.88
IIW-1823-07 [31]	-	5.21×10^{-13}	3.00

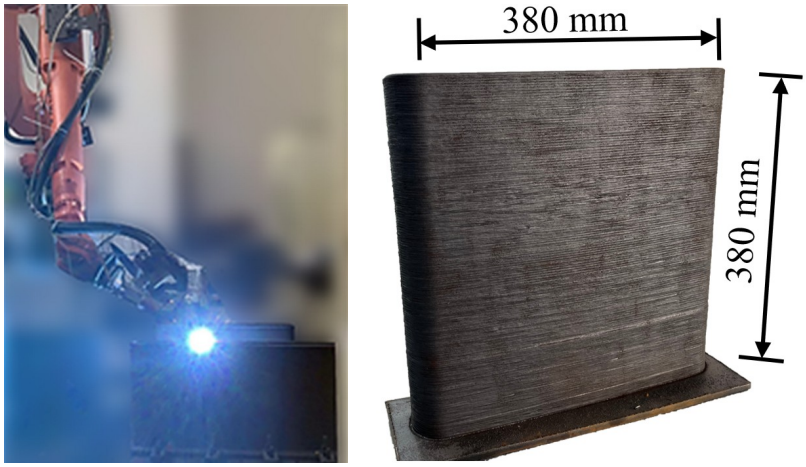

Fig. 1 WAAM 316L austenitic stainless steel oval tubes

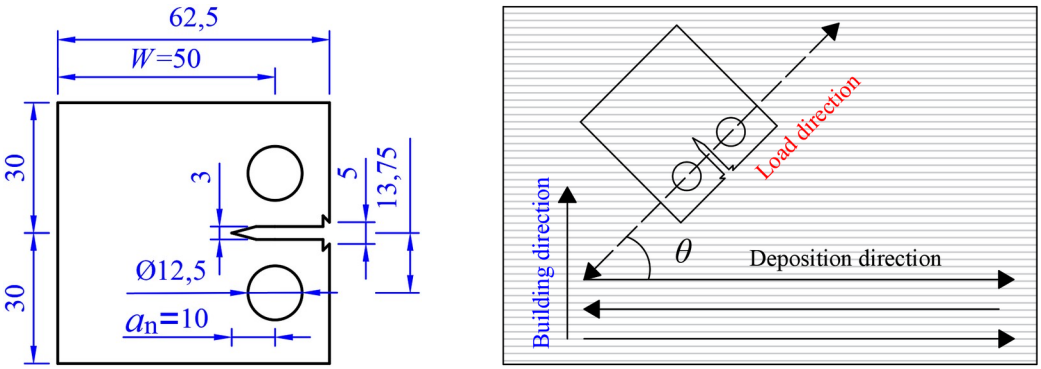

(a) Dimensions of CT specimen (b) Definition of load direction

Fig. 2 Detailed design of CT specimens (dimensions in mm)

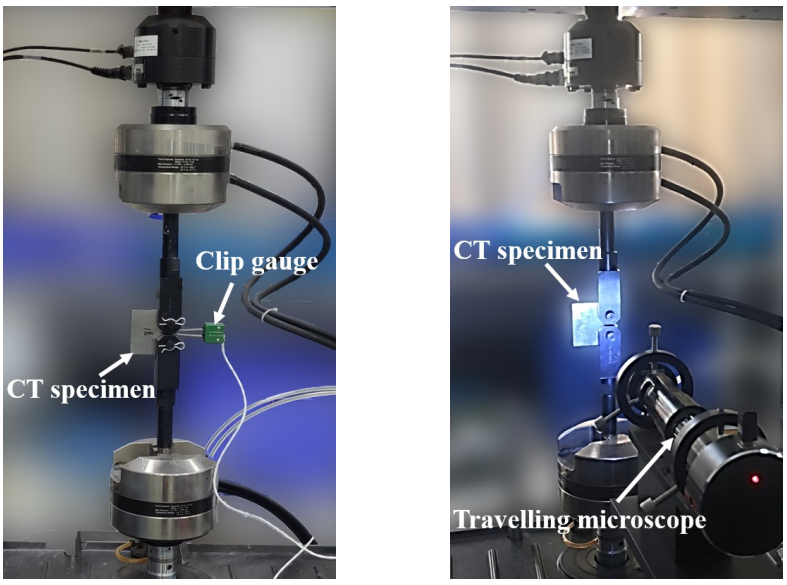

(a) Compliance method (b) Optical method

Fig. 3 Fatigue crack growth test setup

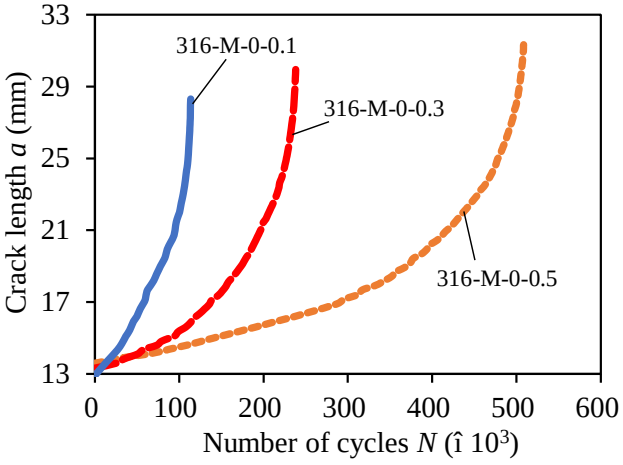

(a) θ = 0° with different load ratios

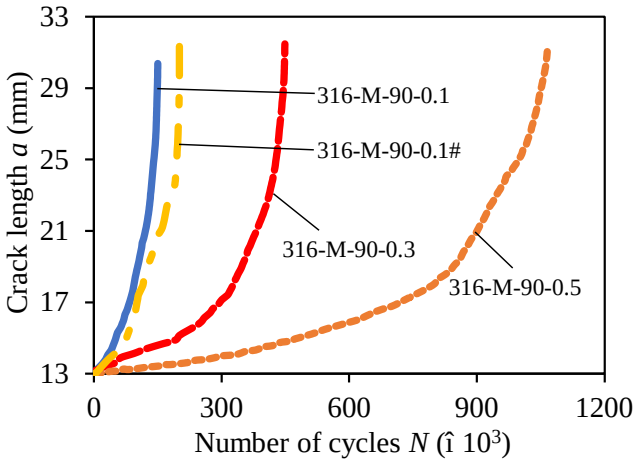

(b) θ = 90° with different load ratios

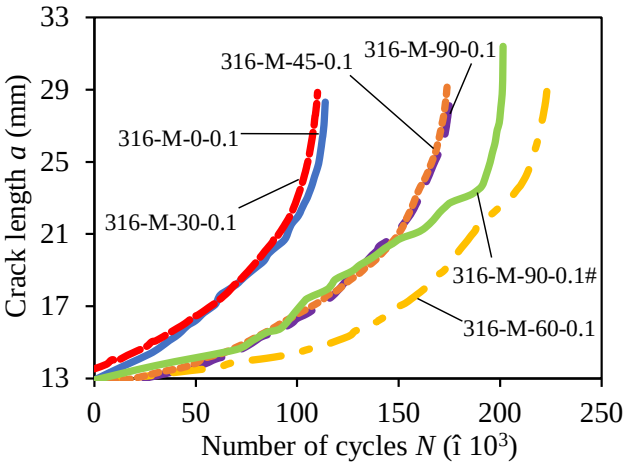

(c) R = 0.1 with different load directions

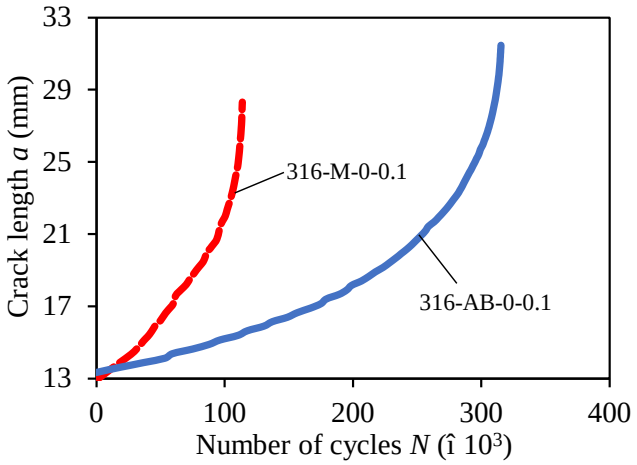

(d) Different surface conditions

Fig. 4 The *a*-*N* curves of WAAM 316L austenitic stainless steel CT specimens

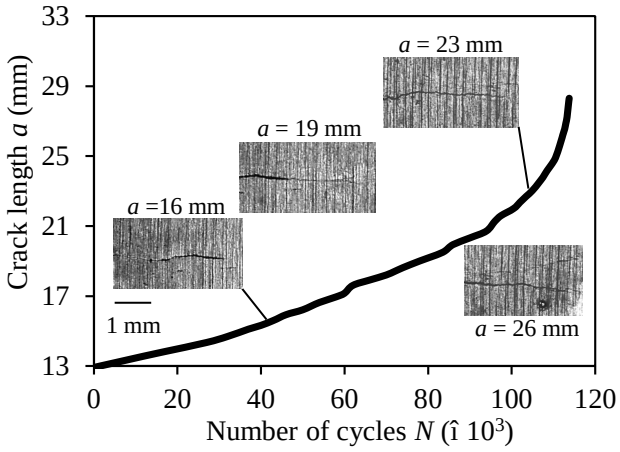

Fig. 5 Fatigue crack growth path and the corresponding *a*-*N* curve of typical specimen 316-M-0-0.1

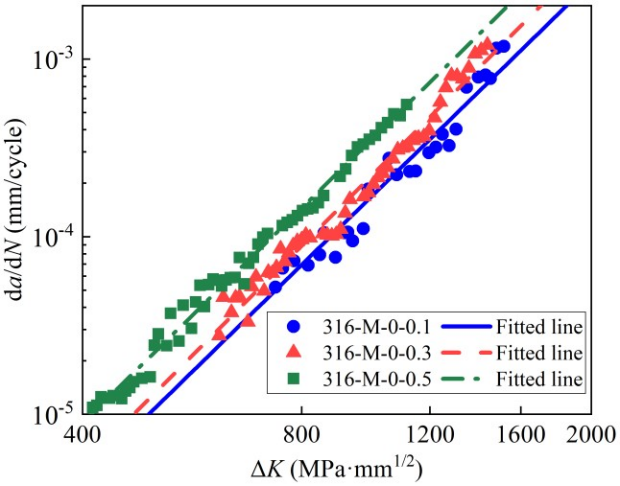

(a) θ = 0° with different load ratios

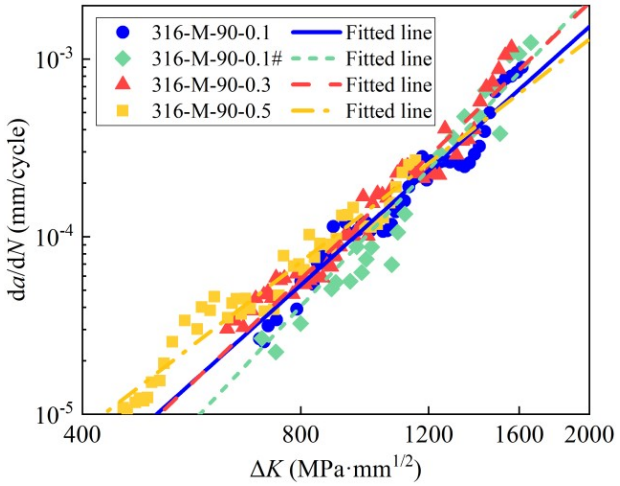

(b) θ = 90° with different load ratios

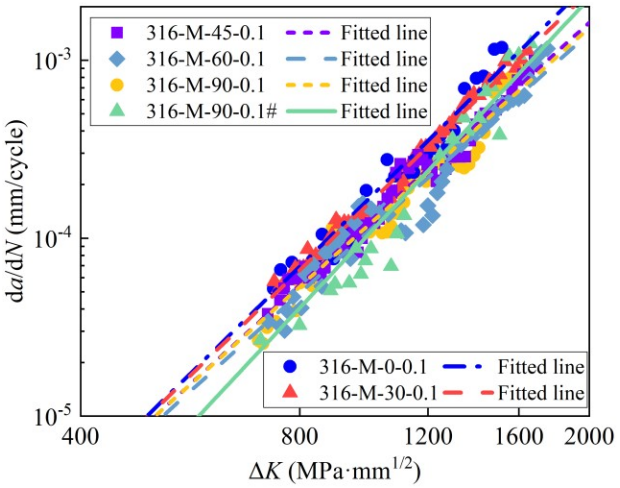

(c) R = 0.1 with different load directions

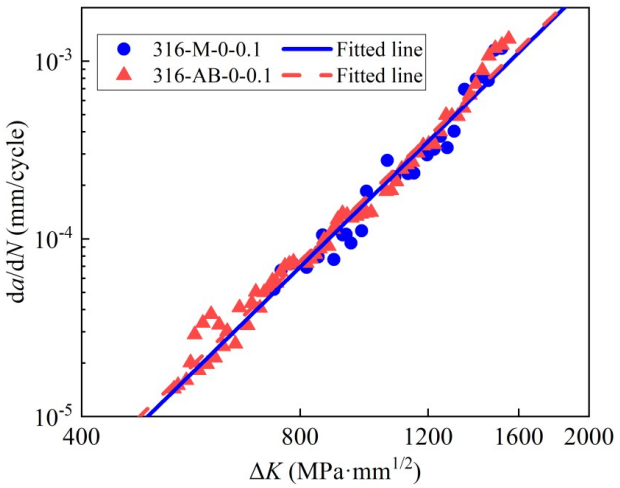

(d) different surface conditions

Fig. 6 The da/dN-ΔK data of WAAM 316L austenitic stainless steel CT specimens and the corresponding fitted lines

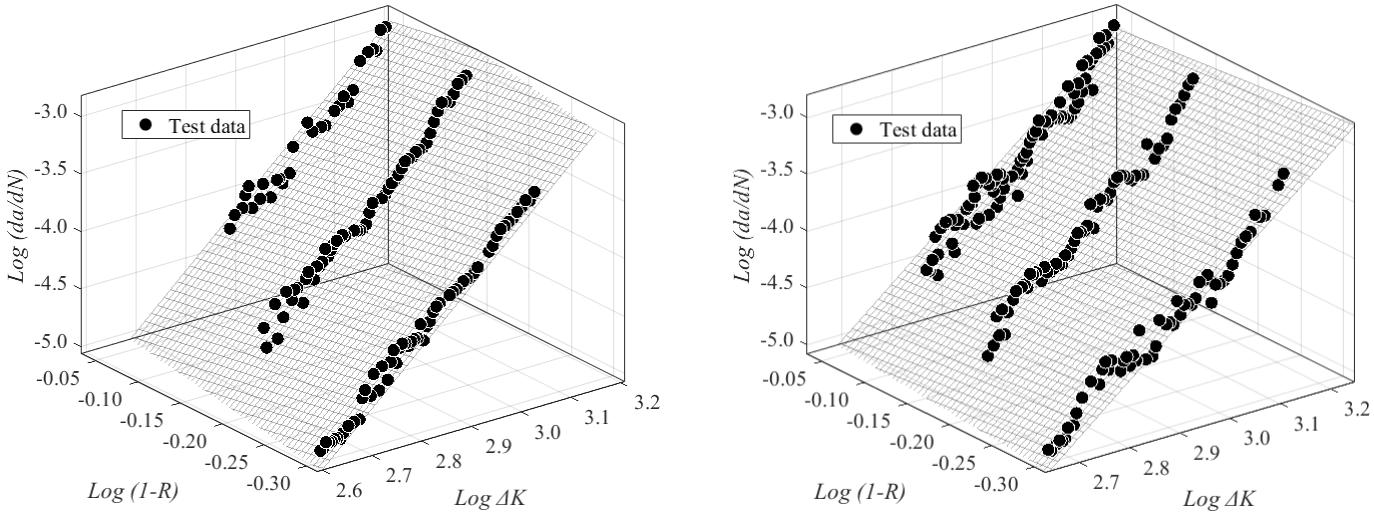

(a) θ = 0° with different load ratios (b) θ = 90° with different load ratios

Fig. 7 The log (da/dN)-log (1-R)-log ΔK data and the corresponding fitted surface

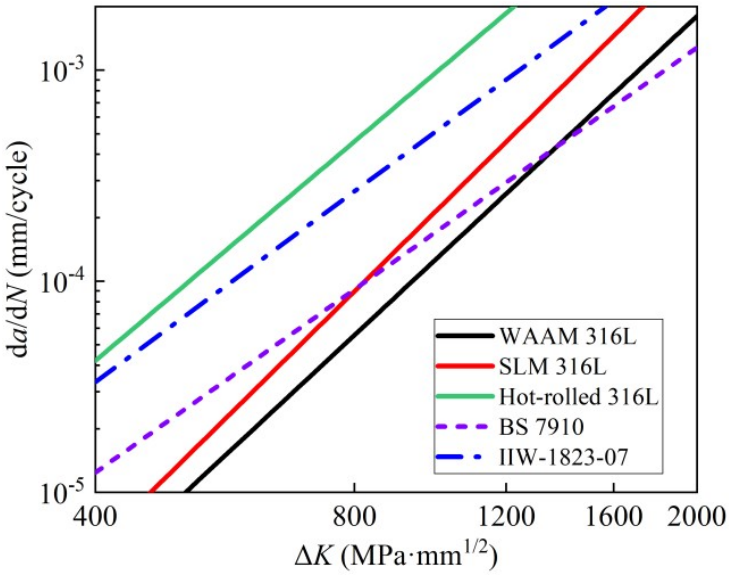

Fig. 8 The da/dN-ΔK relationships of 316L stainless steels by different manufacturing methods and predictions by current standards

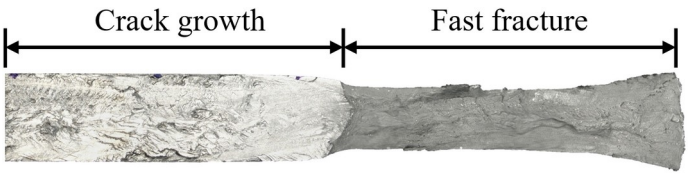

(a) Specimen 316-M-0-0.1

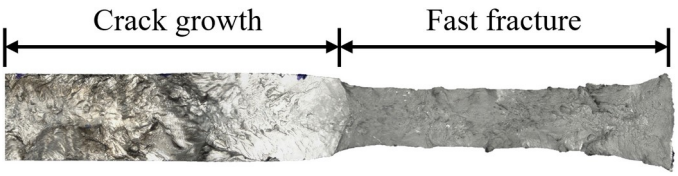

(b) Specimen 316-M-90-0.1#

Fig. 9 Macroscopic fracture surfaces of typical WAAM 316L specimens

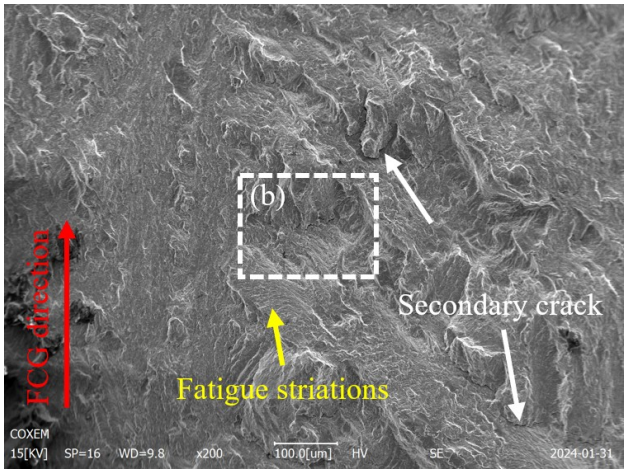

(a) a = 14 mm (× 200)

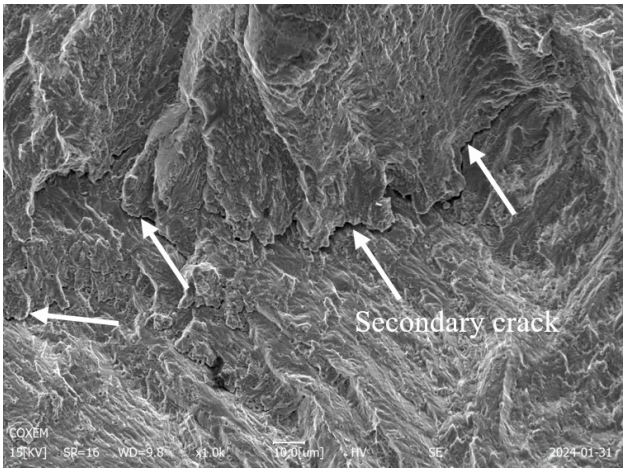

(b) a = 14 mm (× 1000)

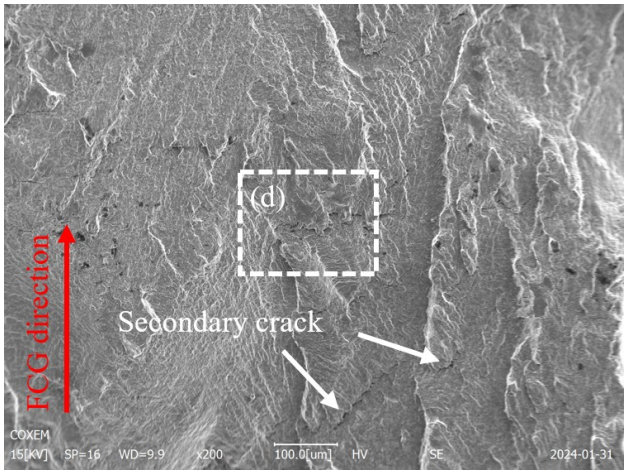

(c) a = 21 mm (× 200)

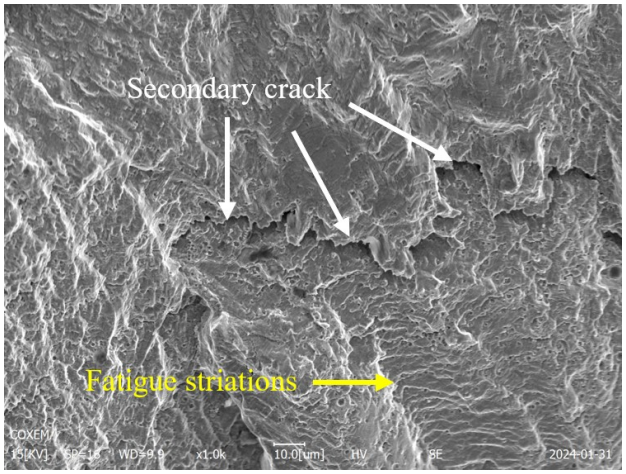

(d) a = 21 mm (× 1000)

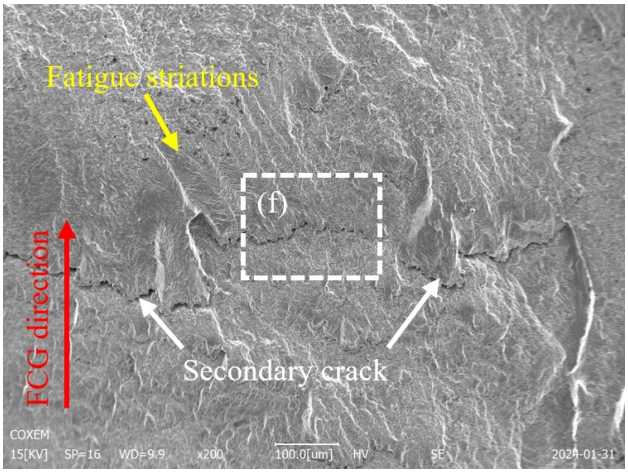

(e) a = 28 mm (× 200)

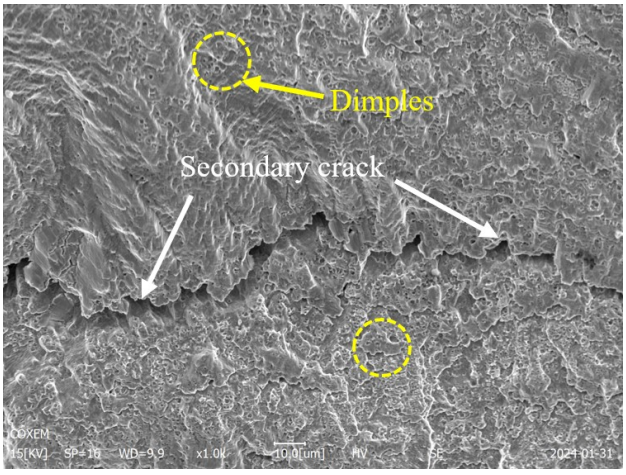

(f) a = 28 mm (× 1000)

Fig. 10 Microscopic fractographies of typical WAAM 316L specimen 316-M-0-0.1

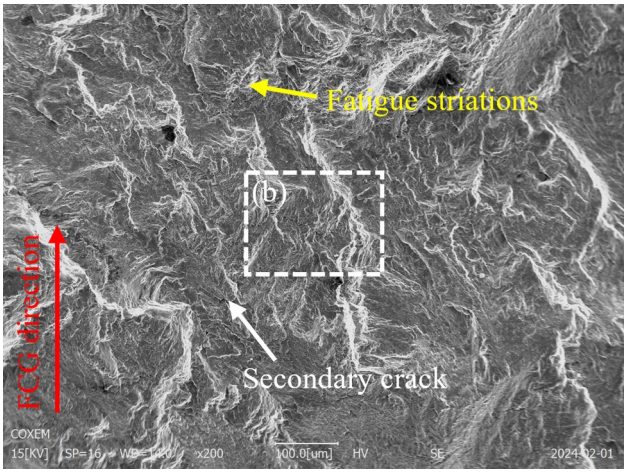

(a) a = 14 mm (× 200)

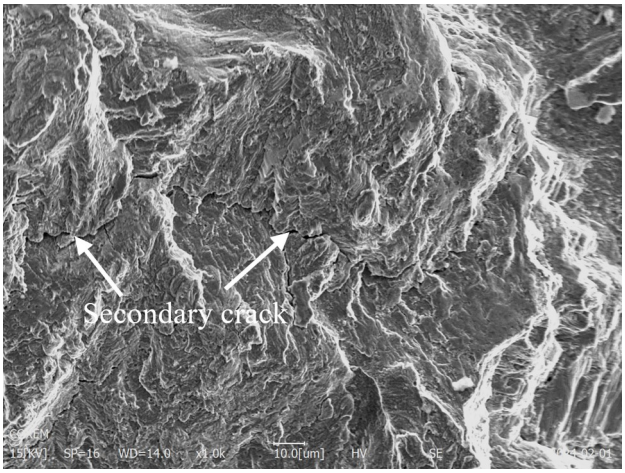

(b) a = 14 mm (× 1000)

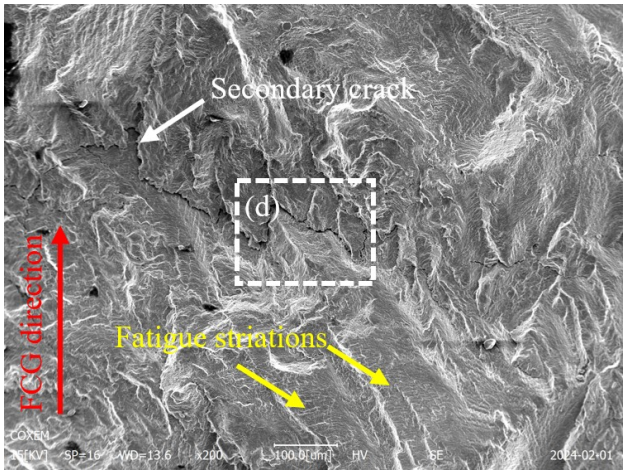

(c) a = 21 mm (× 200)

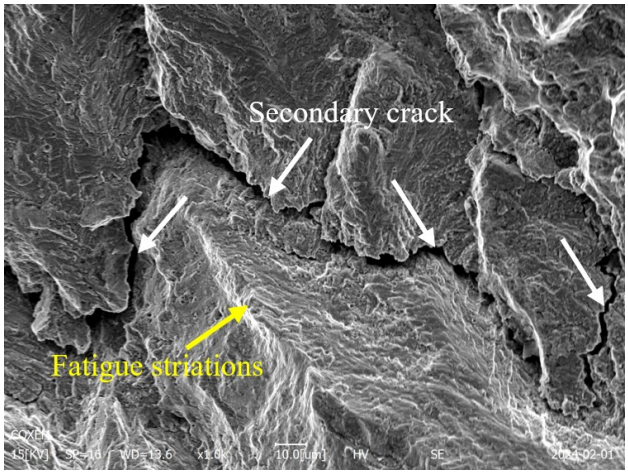

(d) a = 21 mm (× 1000)

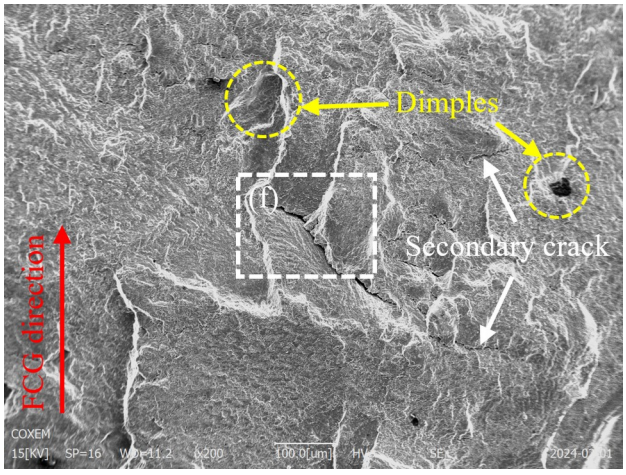

(e) a = 28 mm (× 200)

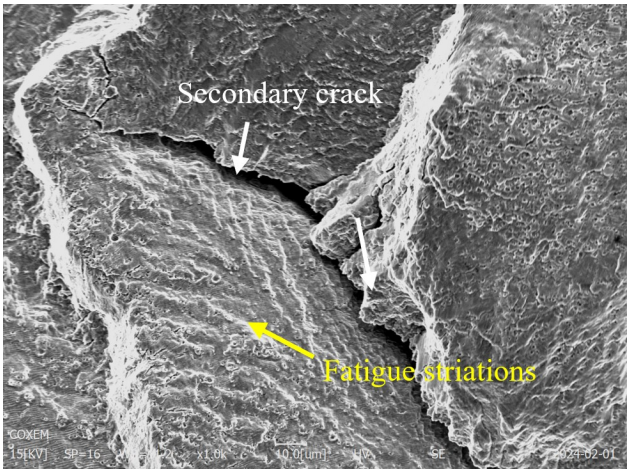

(f) a = 28 mm (× 1000)

Fig. 11 Microscopic fractographies of typical WAAM 316L specimen 316-M-90-0.1#